ORIGINAL PAPER

Influence of submerged sill on the deposition and energy dissipation of granular flow

Gang Luo[1] · Wei Chen[1] · Weigang Shen[1] · Huiao Zhang[2]

Abstract

The large-volume and high-speed channelized granular flows transformed from energetic rockslides and rockfalls are serious geological disasters. The submerged sills embedded in the bedrock and immersed in a granular flow are widely used as a prevention measure in the midstream and downstream of the gullies due to their advantages of high shear resistance, good energy dissipation, and easy cleaning. However, the influence of the geometric characteristics of the submerged sill on the energy dissipation of the granular flow is still not elucidated. Herein, the volume-, velocity-, and runout-reduction effects of the granular flow by the different geometric submerged sill (rectangular, triangular, and cambered) and the geomorphic characteristics of the deposit were studied through physical modeling tests and numerical simulation tests. The results show that: (1) the rank of energy dissipation capacity of submerged sills with different shapes follows the order of cambered > rectangular > triangular; (2) the height of the submerged sill can facilitate the energy dissipation and velocity reduction, especially when the height increases to nearly the depth of the flow; (3) the energy consumption in the interaction process can be attributed to the friction between the particles and sill, the friction between the subsequent mobile particle and stagnant one on the dead zone, and the enhanced collision of the particles during the overflow. The research could provide helpful guidance for disaster prevention and mitigation of channelized granular flow in mountainous areas.

Keywords Channelized granular flow · Submerged sill · Flume modeling test · Numerical simulation · Energy dissipation mechanism

Introduction

Large-scale rockfall or rockslide initiating from the catchment area of high-altitude gullies can fiercely fragment and pulverize during the transportation process and transfer to a high-speed and long-runout avalanche or granular flow (Shugar et al. 2021; Li et al. 2022; Luo et al. 2023). The fluid-like granular flow tends to exhibit longer runout, stronger impacts, and wider coverage, causing extremely serious disasters (Xu et al. 2012; Li et al. 2021). Mitigation strategies refer to protecting the potentially hit areas by passive structures for intercepting, blocking, or changing the motion path of the granular, including check dam, slit dam, flexible barrier, and baffle pile array (Santi et al. 2011; Vagnon 2020; Huang and Zhang 2022).

Instead of a single and large terminal barrier just before the protection target, multiple barriers have been extensively used because they can progressively arrest granular and dissipate energy by creating a cascading effect (Bi et al. 2018; Ng et al. 2022, 2022). Since the baffle pile array has demonstrated exceptional performance in reducing debris disasters, many researchers have conducted a series of experiments and tests to reveal the interaction mechanism and improve its protection capabilities. Choi et al. (2015) analyzed the effectiveness of barrier piles against high-speed debris flows and studied the impact of pile height, layout, and spacing on energy dissipation using the discrete element method. Ng et al. (2015) conducted a series of experiments to investigate the effects of various factors such as the baffle array height, number of rows, spacing between rows, and transverse blockage on the flow velocity of a debris flow. It was found that a single row of baffles had a small effect on reducing the

✉ Gang Luo
  luogang@home.swjtu.edu.cn

[1] Department of Geological Engineering, Faculty of Geosciences and Environmental Engineering, Southwest Jiaotong University, Chengdu 610031, China

[2] China Railway Engineering Design and Consulting Group Co., Ltd, Beijing 100055, China

velocity of the debris flow, and three arrays of baffles can reduce the flow velocity by 57%. Law et al. (2016) studied the effectiveness of installing baffles in front of rigid barriers through flume experiments and DEM simulation. The results showed that the configuration involving the row number, row spacing, and baffle height has an impact on their interception efficiency. Significantly, it was noted that baffles with a height greater than 1.5 times the flow depth will not decrease the peak impact force (Choi et al. 2014; Law et al. 2016). Similarly, Zhang et al. (2021) also studied the velocity deceleration effect of baffle configuration on granular flow and emphasized that the energy dissipation caused by the baffles located on the slope is 60.97% greater than that of the ones on the flat area. Li et al. (2020) used a material point method (MPM) to investigate how the geometry and arrangement of baffles affect the movement and deposition of granular flows, where the baffle efficiency increased with the row spacing until the spacing exceeded 4 times the pile width. Goodwin and Choi (20202020) suggested that a double-slit structure with narrow spacing can effectively control the outflow rate and achieve "self-cleaning."

Furthermore, the researchers found that the shape of the obstacles had an effective role in regulating the energy dissipation and deposition area of the granular flow, especially the arc-shaped obstacle (Choi et al. 2017; Wang et al. 2017, 2020, 2021; Bi et al. 2021). Choi et al. (2017) declared that the arc barrier could reduce the rising height of the granular flow on the barrier and prolong the impact duration. Wang et al. (2021) indicated that among three different shaped baffles, namely rectangular, circular, and arc-shaped baffle, the arc-shaped one has the best blocking and energy dissipation effects and is more advantageous in reducing the impact force. Bi et al. (2021) pointed out that arc-shaped baffles are more effective than other shapes, mainly because granular material could produce friction while moving along the arc surface, resulting in additional kinetic energy loss. Overall, a comprehensive understanding of the impact force and energy dissipation differences through adjusting the configuration of mitigation structures has been achieved, which includes factors such as the number of rows, row spacing, height, and shape. Based on previous studies (Choi et al. 2015; Law et al. 2016; Choi and Goodwin 2020), it is recommended that the ratio of baffle pile height to granular flow depth should be in the range of 1–1.5, and the arc-shaped structure is suggested.

The mitigation structures used in engineering practices, especially for narrow and steep channel-type granular flows, are often damaged by the strong impact force or completely filled by deposits. Regarding the application of submerged sills in debris flows, sills can also regulate flow patterns, enhance energy dissipation, and alleviate the impact force of the granular flow. According to Chen et al. (2014), the spacing between staggered indented sills had a significant regulating effect on the velocity of debris flows. Chen et al. (2016) stated that the velocity of debris flows decreased gradually as the length of the sill section along the channel increased. Chen et al. (2018) illustrated that the energy dissipation capacity of the sill increased with an increase in its cross-sectional area.

In fact, submerged sills, as bump-like obstacles immersed in a granular flow, increase the comprehensive roughness coefficient of the channel. Consequently, they can effectively reduce the velocity of the flow and dissipate its kinetic energy. In particular, for granular flows in narrow and steep channels, sills can reduce the impact force on terminal protective structures such as check dams, slit dams, flexible barriers, and baffle pile arrays. However, the way in which the kinetic energy of the granular flow is transformed and attenuated during the interaction process with a sill is not clearly interpreted. In order to reveal the energy dissipation mechanism of sills against granular flows, the kinetic characteristics of the granular interacting with submerged sills of different geometric shapes (rectangular, triangular, and cambered in cross section) were elucidated by physical modeling and numerical simulation tests. Finally, the influence of different factors on the energy dissipation of the granular flow is deeply discussed.

Methods

Physical modeling test

The physical experiment device of this study is built on the basis of the chute designed by Hutter (1993). It consists of a frame structure, an inclined flume, and a horizontal plate (Fig. 1). A 20-cm-wide chute consisting of 40-cm-high sidewalls and a 250-cm-long inclined plate fixed at a 45° inclination is used to produce rapid granular flow. The source container is positioned at the top of the inclined flume with a height of 150 cm above the ground. The horizontal plate with 200 cm in length and 100 cm in width is used as the deposit area.

Unlike large particles, which are dominated by inertial grain collision stress, the kinetics of small particles are primarily controlled by frictional contact (Sanvitale and Bowman 2017). Therefore, the fractal dimension may play a role in energy dissipation. The fractal dimension, denoted as D, can be used to characterize the particle size distribution (PSD) and can be obtained from the absolute slope of the double logarithmic plot of particle number against particle size. Considering that the fractal dimension D of actual granular flow ranges from 1.3 to 3.2 (Crosta et al. 2007), the material with fractal dimension $D = 1.5$ is configured by quartz sand. The weight of the material used in the experiment was 8 kg with a volume
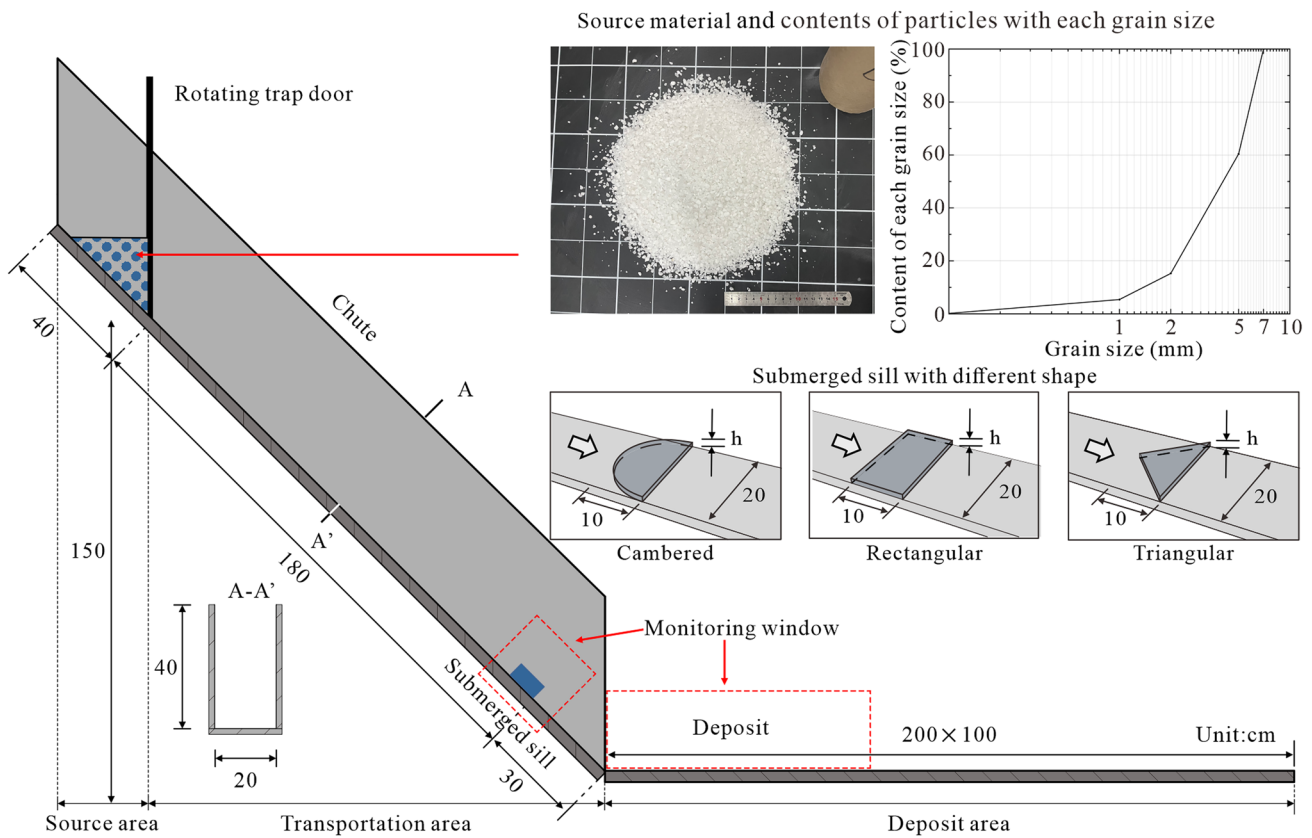
Fig. 1 Chute configuration and test materials of the physical modeling tests

of 3220 cm³. The flow density was assumed to be constant at 2484 kg/m³, which was the measured bulk density in the storage container. The content of each grain size was calculated using Eq. (1), as proposed by Tyler and Wheatcraft (1992) and Hooke and Iverson (1995). The grain size distribution curve of the material is shown in Fig. 1.

$$\frac{M(r < R)}{M_T} = \left(\frac{R}{R_L} \right)^{3-D} \tag{1}$$

where $M(r < R)$ is the mass of particle size less than R, M_T is the total mass, R_L is the upper limitation of particle size, and D is the fractal dimension.

The submerged sill is arranged 30 cm away from the chute port. Three different shapes of submerged sill fabricated by acrylic with the size of 10×20 cm are used in the test: cambered, rectangular, and triangular with a height h of 1 cm, 2 cm, and 4 cm, respectively (Fig. 1). In general, the geometry and height of the submerged sill are considered in the physical experiment, and 6 physical experiments are carried out (Table 2). In this study, the sills are considered completely rigid and are assumed to not consume any flow energy, both experimentally and numerically.

The material is released from the source container and slides down rapidly, eventually accumulating on the horizontal plate. A camera with a rate of 850 frames per second is installed on the side of the submerged sill to record the flow velocity and flow state when the granular particles pass through. Another digital camera is installed on the top of the deposit area to photograph the morphology of the deposits. The velocity distribution and flow pattern are obtained using PIV technology. The 3D morphology of deposits is reconstructed by ContextCapture software, which has the function of aerial triangulation. This software can construct a surface model using images of the deposits from various aerial viewpoints and the coordinates of six measured control points.

Numerical simulation

Since the key physical phenomena within the granular flow cannot be observed by a physical model test, PFC³ᴰ, as a particle discrete element program, is adopted to simulate the kinetics of granular flow and observe abundant phenomena during the interaction between the granular and the submerged sill. In the simulation, a linear contact model is used, which considers both friction and damping between particles (Fig. 2). This model divides the contact force into two
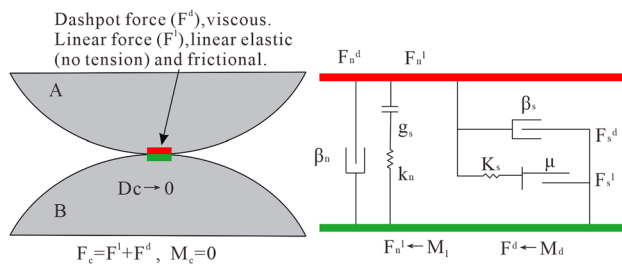
Fig. 2 Behavior and rheological components of the linear model (PFC.^{3D}, Itasca, 2014)

components: linear elastic and viscous. The linear force F^l is generated by a linear spring with constant normal and shear stiffness; the viscous force F^d is produced by dashpots with the normal and shear critical-damping ratio. The numerical model adopts the same channel and baffle configuration as the flume experiments. And the submerged sill is regarded

as rigid in simulation. Table 1 presents the main parameters assigned in the numerical simulation. These parameters were calibrated using various sources of experimental data, including a lifting cylinder test (Fig. 3), a tilting plane test, and physical modeling tests, as well as previous studies by Li et al. (2012), Jiang and Towhata (2013), Scaringi et al. (2018), and Doan et al. (2023). For the simulation, a total of 39,580 spherical particles with a density of 2650 kg/m^3 and the same volume of the experimental sources are generated. Under the action of gravity (9.8 m/s^2), the particles surged downslope and interacted with the sill, gradually accumulating in the deposit area. As presented in Table 2, a total of 13 sets of numerical simulation experiments are conducted.

Numerical model validation

According to Shen et al. (2018) and Ng et al. (2017), dynamic similarity is attained by adopting the Froude number ($Fr = v/\sqrt{ghcos\theta}$), where v is the flow front

Table 1 Input parameters for PFC^{3D}

Input parameter	Value	Calibration
Number of spherical elements	39,580	Generating the same volume of experimental source and the same particle size distribution
Ball density (kg/m^3)	2650	Measured by the experimental material
Effective modulus (MPa)	380	Li et al. (2012)
Ball-ball friction coefficient	0.57	Measured by a lifting cylinder test
Ball-wall friction coefficient	0.51	Measured by a tilting plane test
Normal critical damping ratio	0.2	Scaringi et al. (2018)
Shear critical damping ratio	0.1	Scaringi et al. (2018)

Fig. 3 Comparison between the experimental results and the simulation results by a lifting cylinder test. **a** and **b** particles in the cylinder with the same volume and grading curve and **c** and **d** the same ball-ball friction angle of the deposits, validating the appropriateness of the friction and damping parameters
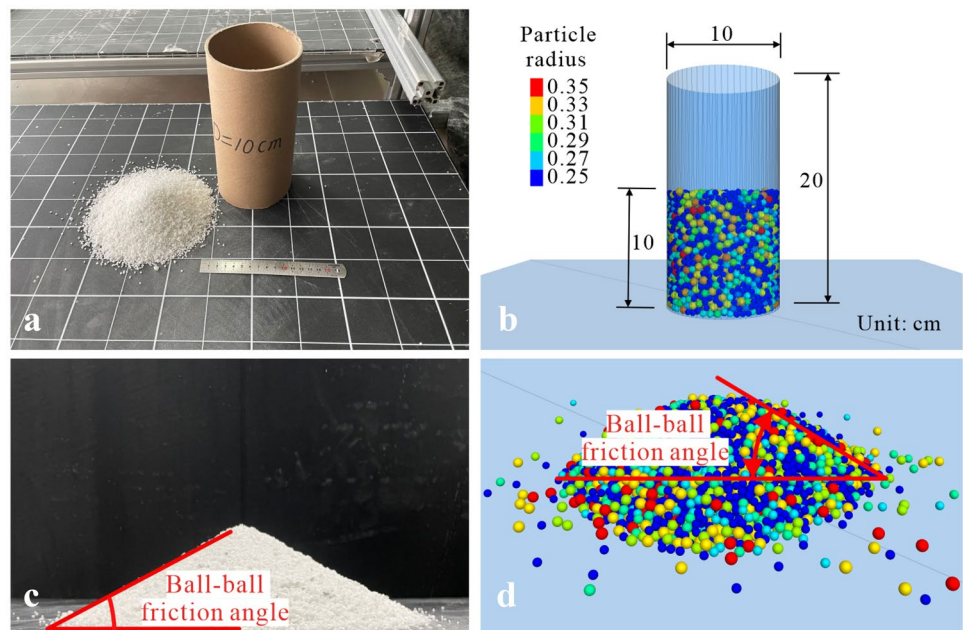
Table 2 Scheme of physical and numerical tests

Methods	Test ID	Geometry of submerged sill	Height (cm)
Physical modeling	P-N-H0	Null	$h=0$
	P–T-H1	Triangular	$h=1$
	P-R-H1	Rectangular	$h=1$
	P–C-H1	Cambered	$h=1$
	P–C-H2	Cambered	$h=2$
	P–C-H4	Cambered	$h=4$
Numerical simulation	N–N-H0	Null	$h=0$
	N-T-H1	Triangular	$h=1$
	N-T-H2	Triangular	$h=2$
	N-T-H3	Triangular	$h=3$
	N-T-H4	Triangular	$h=4$
	N-R-H1	Rectangular	$h=1$
	N-R-H2	Rectangular	$h=2$
	N-R-H3	Rectangular	$h=3$
	N-R-H4	Rectangular	$h=4$
	N–C-H1	Cambered	$h=1$
	N–C-H2	Cambered	$h=2$
	N–C-H3	Cambered	$h=3$
	N–C-H4	Cambered	$h=4$

Table 3 Characteristics of the granular flow for numerical simulation and experimental test

Characteristic	Front velocity v (m/s)	Flow depth h (cm)	F_r
Experiment	3.6	2.5	8.7
Simulation	3.5	2.4	8.6

velocity, h is the depth of the flow, g is the gravitational acceleration, and θ is the inclination of the chute. In this paper, v and h are measured when the granular flow moved to the front of the submerged sill, and the Froude number of experiment and simulation are 8.7 and 8.6, respectively (Table 3).

In order to ensure the consistency between the numerical simulation results and the physical experiments, the reliability is verified based on the geomorphic characteristics and kinetic process (Fig. 4). As shown in Fig. 4a, the granular flow accelerates continuously in the chute due to the gravity from 0.25 to 0.75 s; the flow rushes out of the chute at 1.0 s and accumulates at 1.25 s, which is the same as the experimental result. Because the deposit geomorphology and motional time in the simulation are the same as the physical modeling experiments (Fig. 4b and c), it can be regarded that the simulation method is reasonable and applicable.

Analysis of physical experimental and numerical results

Interaction between granular flow and sill

By studying the flow pattern of the granular flow over the submerged sill, it can be better understood the interaction process. Figure 5 shows the observed impact kinematics of the granular flow interacting with the cambered submerged sill for test P–C-H1 in chronological order. Time starts from the front of the granular flow entering the camera range. The front flow impacts the cambered sill at $t=0.25$ s and overflows it at $t=0.33$ s. The front velocity v and the depth h of the flow measured at $t=0.25$ s are 3.6 m/s and 2.5 cm, respectively (Fig. 5). From $t=0.55$ s to $t=0.70$ s, the granular flow exhibits a stable jet-like run-up with a consistent angle of 25° (Fig. 5). The side view shows clear evidence of segregation, with coarse particles agitating in the front and upper part of the flow and easily saltating over the sill, as observed in the experiment by Ng et al. (2017). In the final stage of flow, fine particles concentrating in the rear of the granular flow gradually overflow the sill or deposit in front of the sill from $t=0.85$ s to $t=1.00$ s. Significantly, the dense laminar flow became the turbulent flow during the overflow process, which enhanced the interactions between particles (Faug 2021).

The process of granular flow flowing over the sill in numerical simulation is investigated, which benefits to understand the deceleration effect of the sill. As shown in Fig. 6, no matter what the geometry of the submerged sill, the velocity-reduction effect is conspicuous. Significantly, the formed dead zone can act as a protective cushion to reduce the impact force and the structural wear caused by granular flow (Bi et al. 2021). Simultaneously, these intercepted particles in the dead zone both reduce the mass of the granular flow and intensify the friction with the subsequent particles climbing the slope of the dead zone. During the climb stage, the energy is consumed by the friction between the passing particles in the flow and stagnant ones as well as the internal collision among the motive particles. Therefore, the longer of the dead zone slope would be more conducive to energy dissipation (Zhang et al. 2020). It is also noteworthy that the velocity of several particles increases due to the diverter effect of the triangular sill in comparison to the rectangular and cambered sills at the beginning ($t=0.875$ s) and end ($t=1.375$ s) of the overflow phase (Fig. 6). Therefore, the topographic jamming effect or fire-hose effect (Morino et al. 2019) that increases the flow velocity induced by the sill should be taken into account in actual engineering. As seen in the blank area on the top surface of the sills (especially for the triangular sill in Fig. 6), the effective contact area between the sill and the particles varied during the overflow and was not
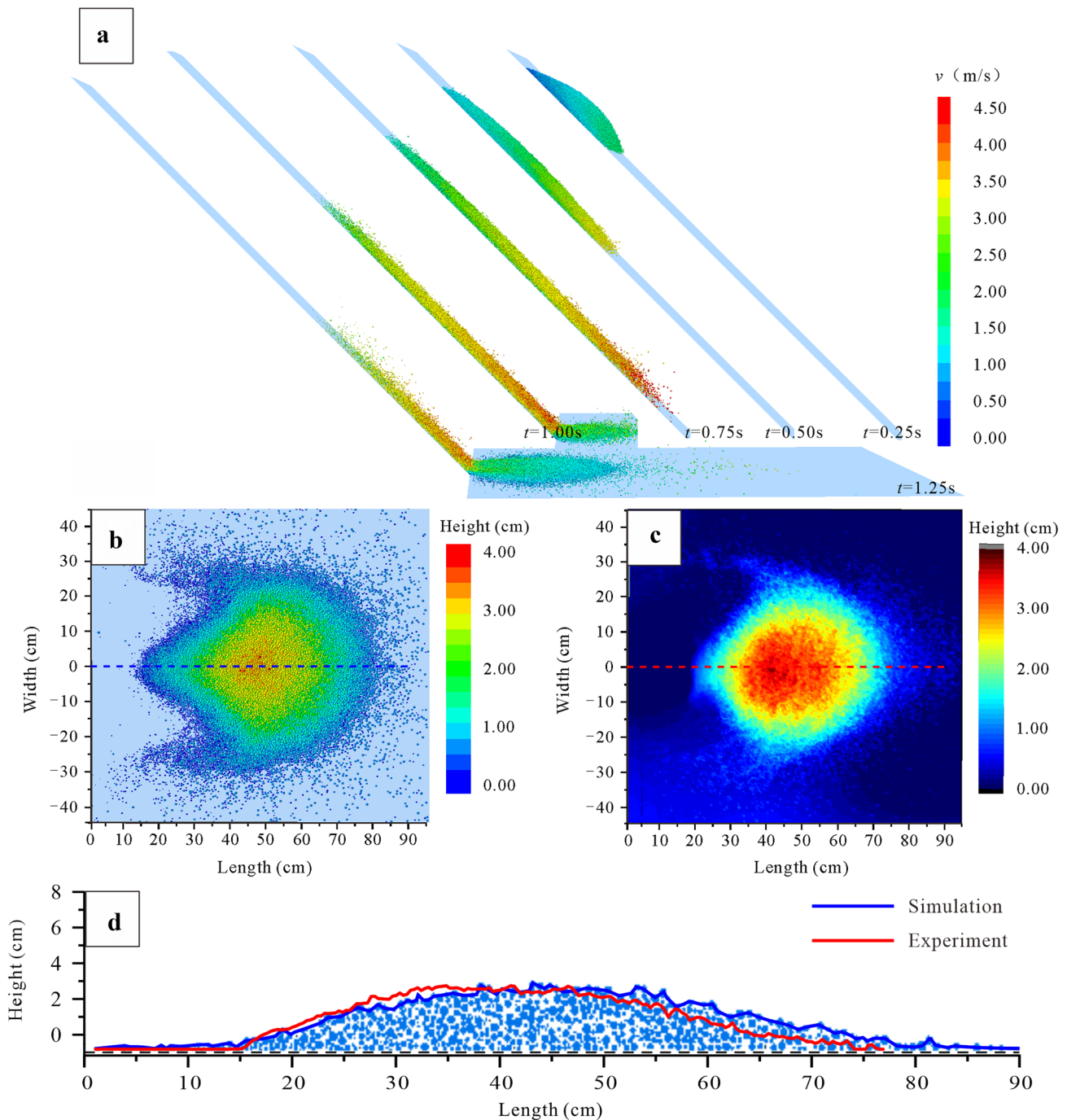
Fig. 4 Validation for numerical simulations. **a** the flow movement of N–N-H0, **b** deposit of N–N-H0, **c** deposit of P-N-H0 by ContextCapture, and **d** the x-axis morphology of deposits in simulation and experiment

equal to the actual area of the sill. In other words, the construction area did not fully contribute to friction due to the constant changes in the flow state and contact mode.

The study also investigates the effect of different heights of the cambered sill ($h = 1$ cm, $h = 2$ cm, and $h = 4$ cm) on the flow-sill interaction. As the height increases, the

flow velocity decreases significantly after flowing over the sill, and the number of stagnant particles increases significantly (Figs. 7 and 8). Figure 8a shows the mass of stagnant particles under different shape sills with the same height, which means the mass-reduction change slightly due to the sill shape. In other words, the volume
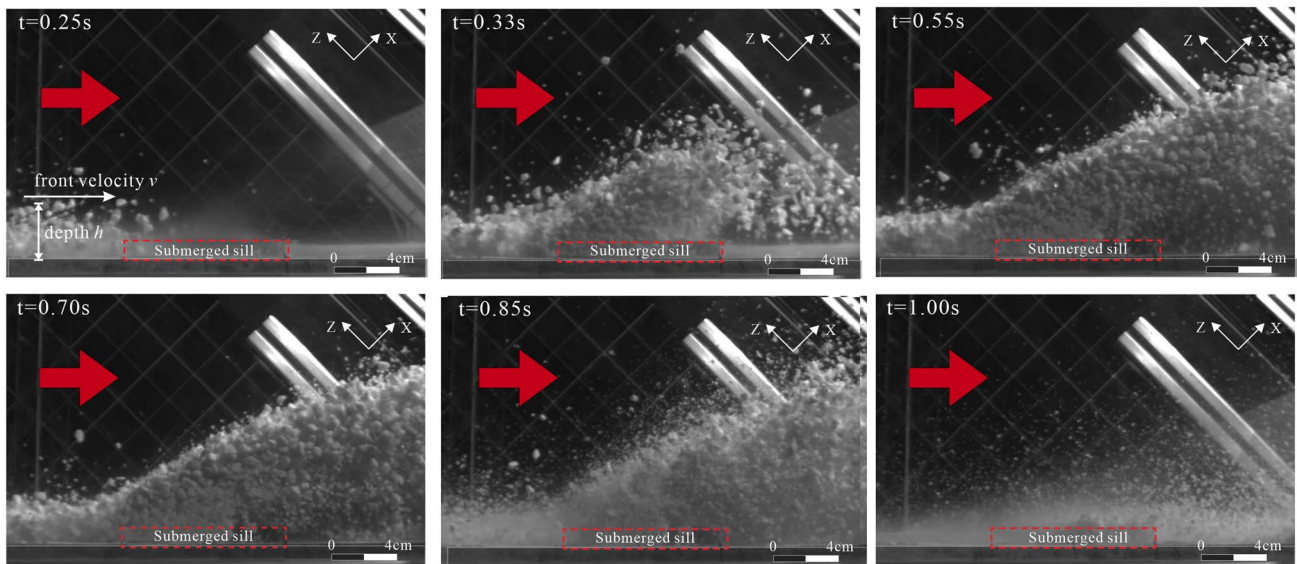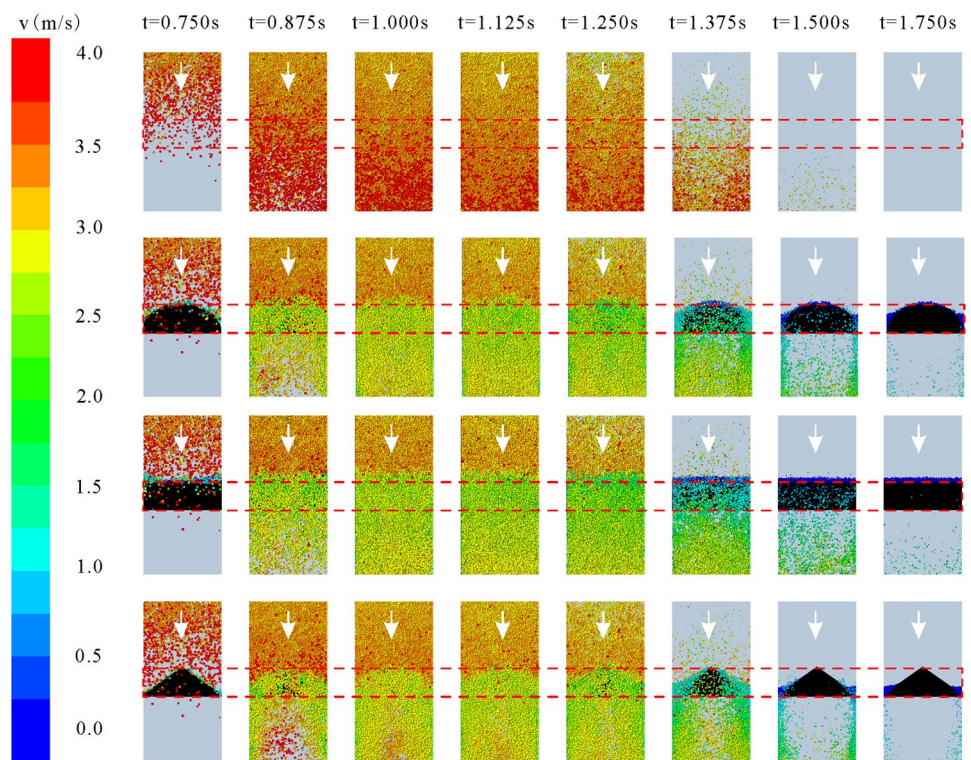
Fig. 5 Side view of the jet-like run-up process of the granular flow

Fig. 6 Kinetic process of granular flow interacting with different submerged sills ($h = 1$ cm)

of dead zones caused by different shape sills is largely identical but with minor differences. Figure 8b shows the mass of stagnant particles under the cambered sill with different height, which manifests that the mass reduction is immensely influenced by the sill height.

Influence of the sill type on the deposition

Because the volume, area, and length of the deposits can indirectly reflect the energy dissipation mode and efficiency of the submerged sills to some extent, the

Fig. 7 Kinetic process of granular flow passing the cambered submerged sill with different heights
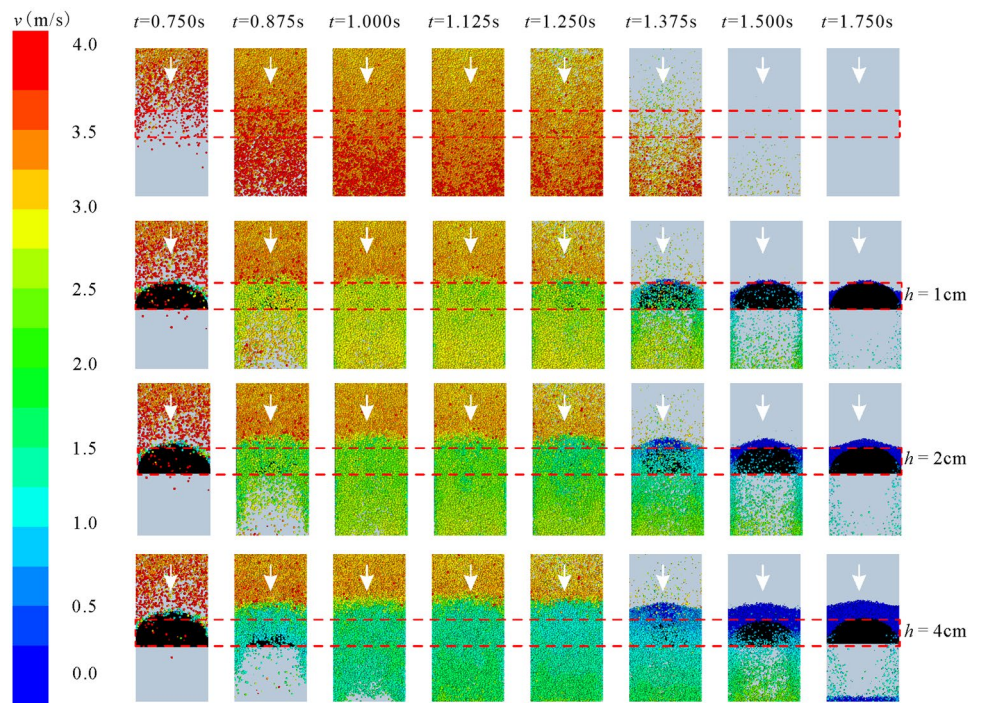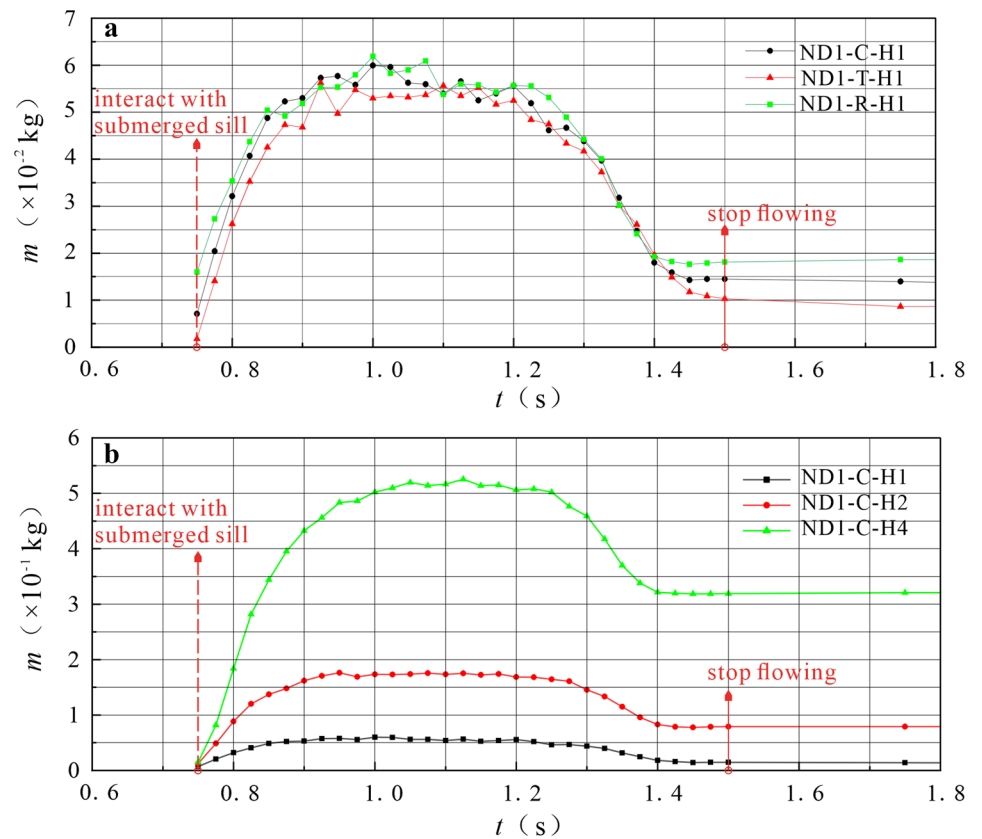

Fig. 8 Mass change of stagnant particles, which are defined as the particles having a velocity of lower than 10% of the average flow velocity. **a** Different geometries and **b** different heights
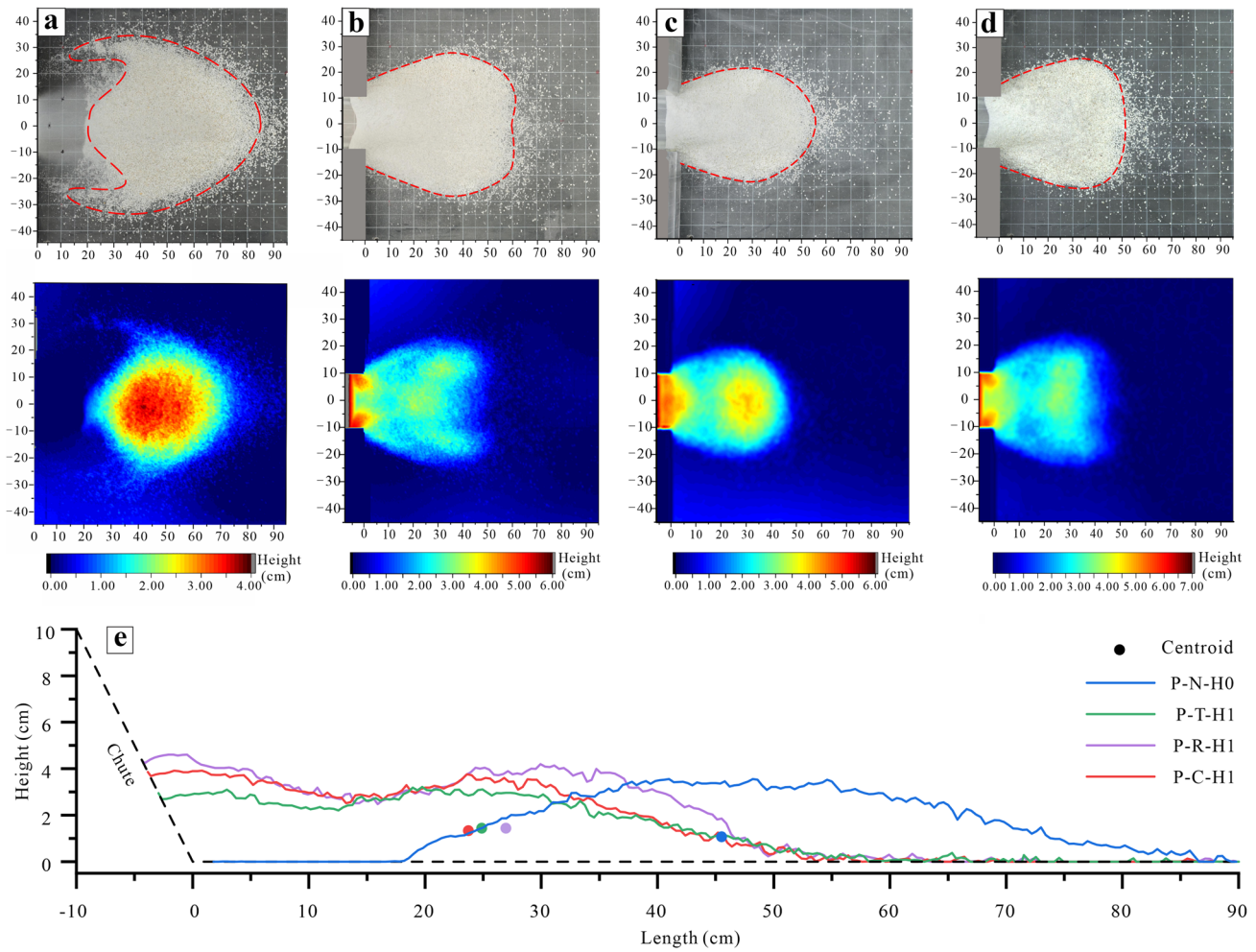
Fig. 9 Morphology of the deposit under different submerged sill types. **a** P-N-H1, **b** P–T-H1, **c** P-R-H1, **d** P–C-H1, and **e** the x-axis morphology of the deposits

Table 4 Morphological parameters of the deposits

Test ID	Deposit area A_d (cm^2)	Maximum thickness T_{max} (cm)	Longitudinal range of deposit L_r (cm)	Transverse range of deposit T_r (cm)	Maximum x-axis coordinate of the deposit X_{max} (cm)	X-axis coordinate of the centroid X_c (cm)
P-N-H0	4109.3	4.2	67.1	70.0	85.1	45.5
P–T-H1	2929.0	3.3	64.0	56.0	58.2	24.9
P-R-H1	2153.5	4.2	50.0	52.0	55.0	27.0
P–C-H1	2341.0	3.5	46.5	52.0	53.5	23.7
P–C-H2	2138.5	-	45.5	47.0	50.5	20.0
P–C-H4	1764.1	-	32.5	42.0	40.5	16.2

morphological parameters of deposits with the three different submerged sills are compared (Fig. 9 and Table 4).

Under the conditions of without submerged sill, cambered, rectangular, and triangular submerged sill, the centroids of the deposit are 45.5 cm, 23.7 cm, 27.0 cm, and 24.9 cm, respectively, and the farthest motion distances are 85.1 cm, 58.2 cm, 55.0 cm, and 53.5 cm, respectively

(Table 4). Compared with the free flow, the runout of the deposit is greatly reduced and the particle accumulation is more concentrated after the submerged sill is installed, indicating a remarkable energy dissipation effect of the sills on the granular flow (Fig. 9). As shown in Table 4 and Fig. 10, the use of cambered submerged sill results in the smallest values for the longitudinal range (L_r), the maximum x-axis
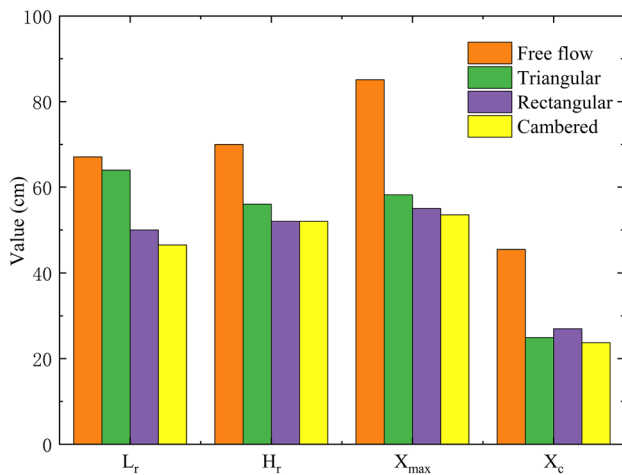
Fig. 10 Comparison of morphological parameters of the deposits under different submerged sill type

coordinate (X_{max}), the centroid (X_c), and the transverse range (T_r) of the deposit. Compared to the case of free flow, the L_r, T_r, X_{max}, and X_c of the deposits under the cambered submerged sill are reduced by 30.7%, 25.7%, 37.1%, and 47.9%, respectively. Overall, the cambered submerged sill exhibits the best energy dissipation capacity among the tested sill shapes.

Influence of the cambered sill height on the deposition

The height of the protection structure is an important factor on preventing supercritical overflow and affecting the energy dissipation of the granular flow (Ng et al. 2015). Normally, with the height increase, more particles accumulate at the chute port, and the deposit area decreases significantly (Fig. 11). Table 4 shows that the maximum x-axis coordinate of the deposit (X_{max}) under the submerged sill height $h=1$ cm, $h=2$ cm, and $h=4$ cm are 53.5 cm, 50.5 cm, and 40.5 cm, respectively, which reduced by 37.1%, 40.7%, and 52.4% compared to the case of free flow. Additionally, the X-axis coordinate of the centroid (X_c) is 23.7 cm, 20.0 cm, and 16.2 cm, corresponding to reduction ratios of 47.9%, 56.0%, and 64.5%, respectively. Therefore, the sill height plays an effective role in mitigating the granular flow.

An important observation is that the jet angle of the granular flow varies significantly depending on the height of the submerged sill. Specifically, for heights $h=1$ cm, $h=2$ cm, and $h=4$ cm, the jet angle is 25°, 40°, and 45°, respectively (Fig. 12). In addition, as the granular flow over the submerged sill, the front velocity decreases from 3.6 to 3.0 m/s for H1, 2.4 m/s for H2, and 2.0 m/s for H4 while passing the submerged sill (Fig. 12). Notably, the higher the sill, the

larger the volume of the dead zone and jet angle, and the more kinetic energy is dissipated.

We compared the energy dissipation effects on granular flow by changing the shape of the sill with changing the height of the sill. In terms of runout distance and centroid position reduction, the differences between different shapes are 5.5% and 7.3%, while the differences between different heights are 15.3% and 16.6% (Table 4 and Fig. 10). Thus, the effect of mitigation by changing the height is greater than that of changing the shape of the submerged sill.

Mechanism of the sill dissipating the granular flow energy

Comprehending the energy change in the interaction process of the granular flow against the submerged sills can help us better understand the energy dissipation mechanism. Because the sill is set to rigidity, the total energy (E_T) of the system consists of three components:

$$E_T = E_G + E_K + E_C \tag{2}$$

where E_G is the gravitational energy, E_K is the kinetic energy, and E_C is the energy dissipation due to damping and friction.

During the whole transportation process of the granular flow, the gravitational energy (E_G) can transform into the kinetic energy (E_K) and eventually dissipated by the friction energy and damping energy (E_C) (Gong et al. 2021; Zhang et al. 2022). From the initiation to the emplacement, the gravitational energy (E_G) of the granular flow continuously reduces due to the altitude loss. Meanwhile, the kinetic energy (E_K) increases as a result of the conversion from the gravitational energy and reaches its peak at 0.78 s (Fig. 13). Compared with the free flow, the sill produces more friction and damping energy consumption, resulting in the kinetic energy loss of the granular flow. This phenomenon can be attributed to the change in flow state from a dense laminar flow to a turbulent flow during the interaction process with the sill, which increases the friction and collision frequency within the particles and leads to a higher energy dissipation rate.

To estimate the energy dissipation of different situations, the reduction rate η of kinetic energy (E_K) is calculated by the following equation and presented in Fig. 14,

$$\eta = \frac{E_{K_{free}} - E_{K_{sill}}}{E_{K_{free}}} \times 100\% \tag{3}$$

where the $E_{K_{free}}$ is the maximum kinetic energy of the free flow, and $E_{K_{sill}}$ is the maximum kinetic energy under different submerged sill type.

Figure 14 shows that the cambered sill with a height of 2 cm exhibits a higher kinetic energy reduction rate compared to other shape sills with a height of 4 cm. This suggests that
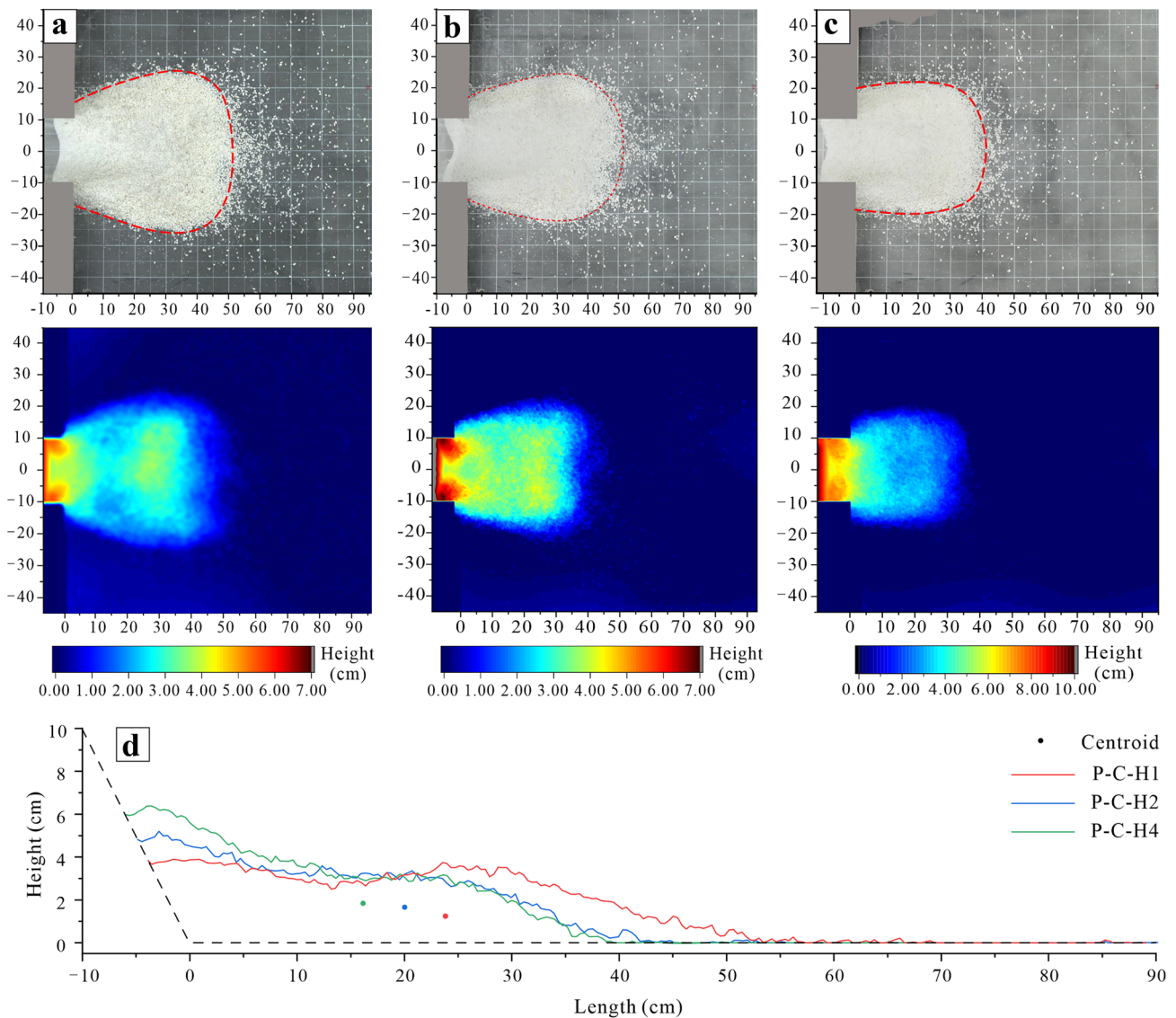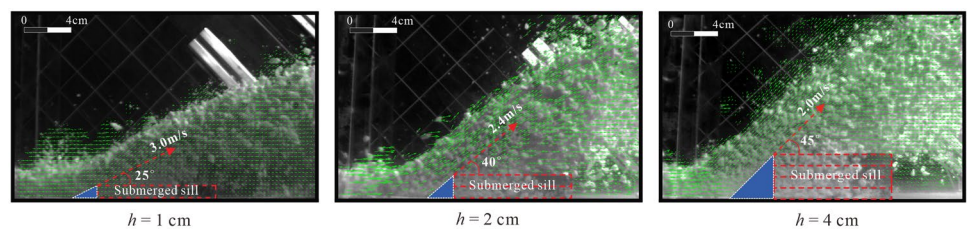
Fig. 11 Morphology of the deposit with different submerged sill heights. **a** P–C–H1, **b** P–C–H2, **c** P–C–H4, and **d** the x-axis morphology of the deposit

Fig. 12 Velocity characteristics of granular flow with different heights

$h = 1$ cm $h = 2$ cm $h = 4$ cm

the cambered sill is more effective in dissipating energy, even at a lower height. Presumably, the different shapes of the sills can create different longitudinal and transverse perturbations in the flow, which in turn increase the frequency and duration of friction and collision within the particles. The triangular sill has the weakest energy dissipation capacity because it only diverts the flow (as shown in Fig. 6) and fails to produce sufficient perturbations. The superior performance of the cambered sill rather than the rectangular one can be attributed to the larger transverse perturbations.
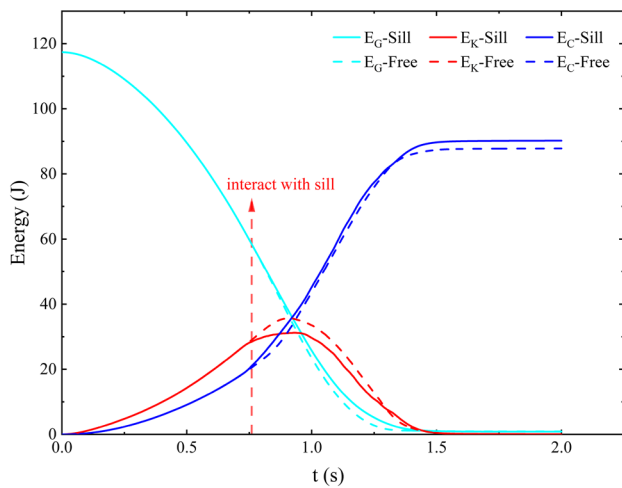
Fig. 13 Energy evolution of the granular flow (three energy components of N–C-H1 and N–N-H0)
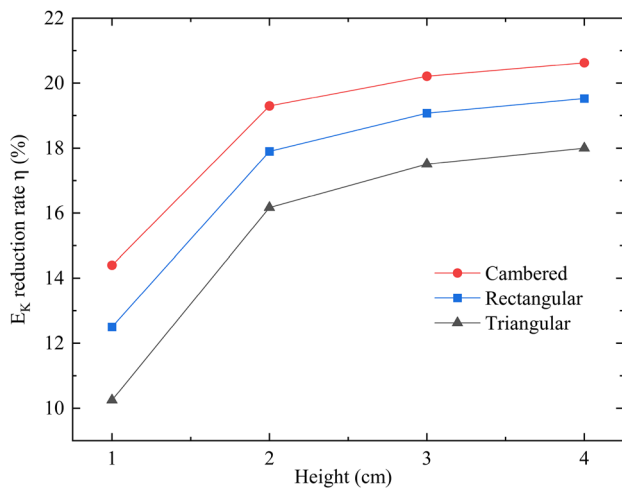

Fig. 14 Kinetic energy reduction rate for different geometries and heights of the sills relative to the free flow

It is interesting to note that the potential contact area (i.e., facing and top surface) has little influence on the energy dissipation in this experiment. Despite the fact that the triangular sill has the largest area ($28.3\,h + 200\ \text{cm}^2$), the cambered sill has a medium-sized area ($31.4\,h + 157\ \text{cm}^2$), and the rectangular sill has the smallest area ($20\,h + 100\ \text{cm}^2$), the cambered sill still performs better than the other shape sills due to its ability to create larger perturbations.

The reduction rate η would have a positive relationship with the submerged sill height. As shown in Fig. 14, when the sill height increases from 1 to 2 cm, the energy reduction rate η has a more significant increase from 14.4 to 19.3%. However, the energy dissipation effect changes slightly when the sill height exceeds 2 cm (Fig. 14), which means the sill

height equal to the depth of the flow has a good energy dissipation capacity.

Since the impact force is a considerable issue to evaluate the mitigation capacity of the sill against the granular flow (Zhang and Huang 2022), the characteristics of the impact force are analyzed herein for the optimization design of the structure. Figure 15a shows the impact force curves on the submerged sill with different shapes, which are smoothed by the Fourier filter (FFT). It was observed that the rectangular sill experienced the strongest impact force from the granular flow (Fig. 15a), mainly due to the normal impact on the sill as opposed to the oblique impact experienced by the cambered and triangular sills. As a result, the triangular and cambered sills can effectively disperse the impact force, reduce local stress concentration, and improve the durability of the structure. Figure 15b shows the impact force on the cambered submerged sill with three different heights. This phenomenon that the impact force is proportional to its height can be explained by the collision frequency, which would intensify due to the increasement of the contact area. In conclusion, the cambered sill shows promising engineering value for mitigating the granular flow and offers the potential for lower costs by reducing both impact capacity and deposit area.

Discussion

Scale is a key issue in the design of the experimental model; the dynamic similarity between the model and the prototype should be considered before the geophysical applications of the granular avalanches model. According to Iverson et al. (2004), ideal granular avalanches represent a limiting case, in which intergranular fluid and cohesion play negligible mechanical roles. Armanini et al. (2011) recognized that the Froude number is the key parameter that influences the impact mechanisms against a rigid obstacle. In this study, the interactions between dry granular flows and submerged sill are investigated, which intergranular fluid is neglected and therefore needs to be studied further. As the Froude number of experiments and simulation $F_r = 8.7$ and 8.6 respectively, the results in this paper are only suitable for granular flow with the Froude number nearly 8.6 in nature.

Taberlet et al. (2003) demonstrated that sidewall friction impacts the kinetics and sedimentation of granular flow in thin channels and proposed an equation (Eq. 4) to evaluate the comprehensive friction coefficient.

$$tan\ \varphi = u_i + u_w \frac{h}{W} \tag{4}$$

where φ is the comprehensive friction coefficient of the granular flow, u_i is a constant internal friction coefficient of
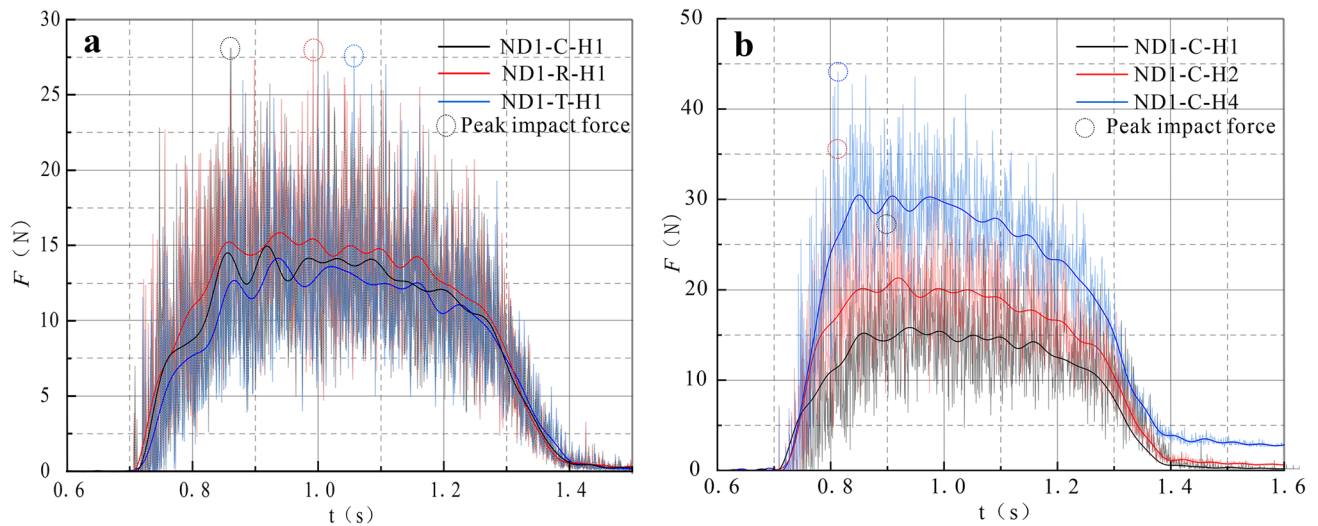
Fig. 15 Impact force on the submerged sill. **a** Different types and **b** different heights

the particle material, u_w is an effective friction coefficient accounting for both sliding and rolling of the particles on the walls, h is the flow depth, and W is the experimental channel width.

In this study, the ball-wall friction coefficient (u_w) is 0.51, the flow depth (h) was 2.5 cm, the channel width (W) was 20 cm, and $u_w \times h/W$ was 0.06375, indicating that the effect of sidewall friction on the granular flow was minimal and could be ignored. More significantly, the core of this paper is to study the impact of the sill on the overall energy consumption of granular flow through a comparative analysis. Assuming that the friction between the particles and the sidewall is roughly equal in situations with and without a sill, the friction effect of the sidewall will be eliminated using the situation without a sill as a baseline.

The mitigation structures in engineering also face the challenge of invalidation due to the supercritical overflow of the granular flow (Huang et al. 2021). In this paper, the jet angle of the supercritical overflow flowing over the submerged sill is observed by PIV analysis (Fig. 12). The jet angle increases to 45° as the height of the submerged

sill increases to 4 cm, which is agree with the conclusion by Hákonardóttir et al. (2003), who found that the angle $\theta + \psi$ increases to an angle close to α as the height of the structure increases. More important, the jet angle θ determines the vertical and horizontal components of the velocity of the granular flow (Fig. 16), which further ascertain the trajectory of the flow including the subsequent impact position and the angle of collision between the flow and the ground. The normal momentum perpendicular to the ground at the next impact would be partly absorbed by the bedrock in the form of elastic–plastic deformation. On the contrary, the tangential momentum along the ground nothing to do with the energy dissipation will push the flow further. Therefore, the jet angle of the flow while passing the sill is another important factor of the energy dissipation, which is associated with the Froude number, grain size, slope of the gully bed, and geometry of the structure. Although our study is primarily concerned with the energy dissipation of granular flows with and without a sill, we recognize that other factors such as overflow characteristics and landing dynamics can also impact the behavior

Fig. 16 Trajectory of the granular flow passing the sill, side-view (according to Hákonardóttir et al. 2003)
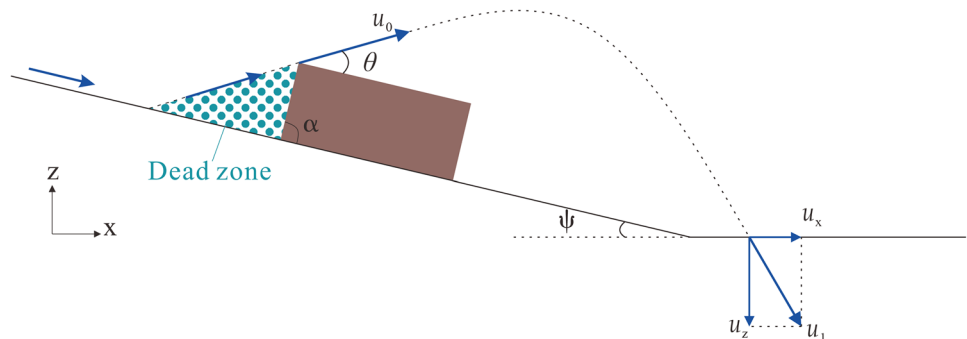
of these flows, which are beyond the scope of our paper. A comprehensive analysis on these issues can be found in Ng et al. (20212023).

Conclusion

In this study, physical modeling and numerical simulation tests are carried out to analyze the influence of the shape and height of the submerged sill on the energy dissipation and deposition characteristics of the granular flow with a Froude number equal to 8.7. The main conclusions are as follows:

1) When compared with free sliding, the submerged sills with cambered, rectangular, and triangular shapes reduce the kinetic energy of the granular flow by 14.4%, 12.5%, and 10.2%, respectively; reduce the runout by 37.1%, 35.4%, and 31.6%, respectively; and reduce the deposit area by 43.0%, 47.6%, and 28.7%, respectively. In conclusion, the submerged sills can be ranked in terms of their energy dissipation capacity for the flow regime ($F_r = 8.7$) in the following order: cambered > rectangular > triangular.

2) Among the three types of sills, the rectangular one bears the highest impact force, as the impact is normal to the sill rather than oblique for the cambered and triangular shapes. Moreover, the impact force is proportional to the sill height due to the increase in contact area.

3) As the height of the submerged sill increases from 1 to 4 cm, the volume-, velocity-, and runout-reduction of the granular flow all increase significantly, while the centroid distance and accumulation area of the deposits decrease noticeably. However, due to the nonlinear effect of the sill height on energy dissipation, a sill height equal to the depth of the flow for optimal energy dissipation is recommended.

4) From an engineering and economic standpoint, increasing the submerged sill height will require more concrete, whereas changing the shape of a sill can be more effective than simply increasing its height in dissipating energy and reducing the impact force on itself without the need for additional materials.

5) The energy dissipation of the granular flow caused by the submerged sills can be attributed to the friction and collision between the particles and the sill, as well as between the subsequent mobile particles and stagnant ones in the dead zone and within the particles themselves. Moreover, the various shapes of the sills can create different longitudinal and transverse perturbations in the flow, which can increase the frequency and duration of friction and collision between the particles, further contributing to the overall energy dissipation.

References

Armanini A, Larcher M, Odorizzi M (2011) Dynamic impact of a debris flow against a vertical wall. Ital J Eng Geol Env 1:2011. https://doi.org/10.4408/IJEGE.2011-03.B-113

Bi Y, Du Y, He S et al (2018) Numerical analysis of effect of baffle configuration on impact force exerted from rock avalanches. Landslides 15:1029–1043. https://doi.org/10.1007/s10346-018-0979-z

Bi Y, Sun X, Zhao H et al (2021) Comparison regarding the effects of different baffle systems as impacted by rock avalanches. Int J Civ Eng 19:127–144. https://doi.org/10.1007/s40999-020-00557-w

Chen X, You Y, Chen J et al (2014) Characteristics of a drainage channel with staggered indented sills for controlling debris flows. J Mt Sci 11:1242–1252. https://doi.org/10.1007/s11629-013-2917-9

Chen J, Chen X, Chen H, Zhao W (2016) Characteristics of viscous debris flow in a drainage channel with an energy dissipation structure. J Mt Sci 13:223–233. https://doi.org/10.1007/s11629-014-3290-z

Chen J, Chen X, Zhao W, You Y (2018) Debris flow drainage channel with energy dissipation structures: experimental study and engineering application. J Hydraul Eng 144:06018012. https://doi.org/10.1061/(ASCE)HY.1943-7900.0001523

Choi CE, Goodwin SR (2020) Interaction between granular flows and flexible obstacles: a grain-scale investigation. Comput Geotech 128:103800. https://doi.org/10.1016/j.compgeo.2020.103800

Choi CE, Ng CWW, Song D et al (2014) Flume investigation of landslide debris–resisting baffles. Can Geotech J 51:540–553. https://doi.org/10.1139/cgj-2013-0115

Choi CE, Ng CWW, Law RPH et al (2015) Computational investigation of baffle configuration on impedance of channelized debris flow. Can Geotech J 52:182–197. https://doi.org/10.1139/cgj-2013-0157

Choi CE, Cui Y, Liu LHD et al (2017) Impact mechanisms of granular flow against curved barriers. Géotech Lett 7:330–338. https://doi.org/10.1680/jgele.17.00068

Crosta GB, Frattini P, Fusi N (2007) Fragmentation in the Val Pola rock avalanche. Italian Alps J Geophys Res 112:F01006. https://doi.org/10.1029/2005JF000455

Doan T, Indraratna B, Nguyen TT, Rujikiatkamjorn C (2023) Interactive role of rolling friction and cohesion on the angle of repose through a microscale assessment. Int J Geomech 23:04022250. https://doi.org/10.1061/(ASCE)GM.1943-5622.0002632

Faug T (2021) Impact force of granular flows on walls normal to the bottom: slow versus fast impact dynamics. Can Geotech J 58:114–124. https://doi.org/10.1139/cgj-2019-0399

Gong S, Zhao T, Zhao J et al (2021) Discrete element analysis of dry granular flow impact on slit dams. Landslides 18:1143–1152. https://doi.org/10.1007/s10346-020-01531-2

Goodwin GR, Choi CE (2020) Slit structures: fundamental mechanisms of mechanical trapping of granular flows. Comput Geotech 119:103376. https://doi.org/10.1016/j.compgeo.2019.103376

Hákonardóttir KM, Hogg AJ, Jóhannesson T, Tómasson GG (2003) A laboratory study of the retarding effects of braking mounds on snow avalanches. J Glaciol 49:191–200. https://doi.org/10.3189/172756503781830692

Hooke RL, Iverson NR (1995) Grain-size distribution in deforming subglacial tills: role of grain fracture. Geology 23:57. https://doi.org/10.1130/0091-7613(1995)023%3c0057:GSDIDS%3e2.3.CO;2

Huang Y, Zhang B (2022) Challenges and perspectives in designing engineering structures against debris-flow disaster. Eur J Environ Civ En 26:4476–4497. https://doi.org/10.1080/19648189.2020.1854126

Huang Y, Zhang B, Zhu C (2021) Computational assessment of baffle performance against rapid granular flows. Landslides 18:485–501. https://doi.org/10.1007/s10346-020-01511-6

Hutter (1993) Motion of a granular avalanche in a convex and concave curved chute: experiments and theoretical predictions. Phil Trans R Soc Lond A 342:573–600. https://doi.org/10.1098/rsta.1993.0033

Itasca Consulting Group Inc (2014) PFC3D: particle flow code in 3 dimensions (version 5.0) Manual. Itasca Consulting Group Inc, Minneapolis, USA

Iverson RM, Logan M, Denlinger RP (2004) Granular avalanches across irregular three-dimensional terrain: 2. Experimental tests. J Geophys Res-Earth 109. https://doi.org/10.1029/2003JF000084

Jiang YJ, Towhata I (2013) Experimental study of dry granular flow and impact behavior against a rigid retaining wall. Rock Mech Rock Eng 46:713–729. https://doi.org/10.1007/s00603-012-0293-3

Law RPH, Choi CE, Ng CWW (2016) Discrete-element investigation of influence of granular debris flow baffles on rigid barrier impact. Can Geotech J 53:179–185. https://doi.org/10.1139/cgj-2014-0394

Li WC, Li HJ, Dai FC, Lee LM (2012) Discrete element modeling of a rainfall-induced flowslide. Eng Geol 149–150:22–34. https://doi.org/10.1016/j.enggeo.2012.08.006

Li X, Yan Q, Zhao S et al (2020) Investigation of influence of baffles on landslide debris mobility by 3D material point method. Landslides 17:1129–1143. https://doi.org/10.1007/s10346-020-01346-1

Li K, Wang Y-F, Lin Q-W et al (2021) Experiments on granular flow behavior and deposit characteristics: implications for rock avalanche kinematics. Landslides 18:1779–1799. https://doi.org/10.1007/s10346-020-01607-z

Li K, Cheng Q, Lin Q, Wang Y et al (2022) State of the art on rock avalanche dynamics from granular flow mechanics. Earth Sci-J China Univ. Geosci 47:893. https://doi.org/10.3799/dqkx.2021.169

Luo G, Chen X, Zhang Q et al (2023) Failure mechanism and sedimentary characteristics of a catastrophic rockslide avalanche induced by the 2008 Wenchuan earthquake. Landslides 20:25–38. https://doi.org/10.1007/s10346-022-01955-y

Morino C, Conway SJ, Balme MR et al (2019) Debris-flow release processes investigated through the analysis of multi-temporal LiDAR datasets in north-western Iceland. Earth Surf Proc Land 44:144–159. https://doi.org/10.1002/esp.4488

Ng CWW, Choi CE, Song D et al (2015) Physical modeling of baffles influence on landslide debris mobility: baffle physical modeling influence on landslide debris mobility. Landslides 12:1–18. https://doi.org/10.1007/s10346-014-0476-y

Ng CWW, Choi CE, Liu LHD et al (2017) Influence of particle size on the mechanism of dry granular run-up on a rigid barrier. Géotech Lett 7:79–89. https://doi.org/10.1680/jgele.16.00159

Ng CWW, Majeed U, Choi CE, De Silva WARK (2021) New impact equation using barrier Froude number for the design of dual rigid barriers against debris flows. Landslides 18:2309–2321. https://doi.org/10.1007/s10346-021-01631-7

Ng CWW, Liu H, Choi CE et al (2022) Effects of basal clearance on the impact dynamics of dry granular flow against dual rigid barriers. Can Geotech J 59:1161–1174. https://doi.org/10.1139/cgj-2020-0682

Ng CWW, Jia Z, Poudyal S et al (2023) Two-phase MPM modelling of debris flow impact against dual rigid barriers. Géotechnique 1–14. https://doi.org/10.1680/jgeot.22.00199

Santi PM, Hewitt K, VanDine DF, Barillas Cruz E (2011) Debris-flow impact, vulnerability, and response. Nat Hazards 56:371–402. https://doi.org/10.1007/s11069-010-9576-8

Sanvitale N, Bowman ET (2017) Visualization of dominant stress-transfer mechanisms in experimental debris flows of different particle-size distribution. Can Geotech J 54:258–269. https://doi.org/10.1139/cgj-2015-0532

Scaringi G, Fan X, Xu Q et al (2018) Some considerations on the use of numerical methods to simulate past landslides and possible new failures: the case of the recent Xinmo landslide (Sichuan, China). Landslides 15:1359–1375. https://doi.org/10.1007/s10346-018-0953-9

Shen W, Zhao T, Zhao J et al (2018) Quantifying the impact of dry debris flow against a rigid barrier by DEM analyses. Eng Geol 241:86–96. https://doi.org/10.1016/j.enggeo.2018.05.011

Shugar DH, Jacquemart M, Shean D et al (2021) A massive rock and ice avalanche caused the 2021 disaster at Chamoli, Indian Himalaya. Science 373:300–306. https://doi.org/10.1126/science.abh4455

Taberlet N, Richard P, Valance A et al (2003) Superstable granular heap in a thin channel. Phys Rev Lett 91:264301. https://doi.org/10.1103/PhysRevLett.91.264301

Tyler SW, Wheatcraft SW (1992) Fractal scaling of soil particle-size distributions: analysis and limitations. Soil Sci Soc Am J 56:362–369. https://doi.org/10.2136/sssaj1992.03615995005600020005x

Vagnon F (2020) Design of active debris flow mitigation measures: a comprehensive analysis of existing impact models. Landslides 17:313–333. https://doi.org/10.1007/s10346-019-01278-5

Wang F, Chen X, Chen J, You Y (2017) Experimental study on a debris-flow drainage channel with different types of energy dissipation baffles. Eng Geol 220:43–51. https://doi.org/10.1016/j.enggeo.2017.01.014

Wang D, Li Q, Bi Y, He S (2020) Effects of new baffles system under the impact of rock avalanches. Eng Geol 264:105261. https://doi.org/10.1016/j.enggeo.2019.105261

Wang D, Bi Y, Li Q, He S (2021) Kinetic response analysis of different types of baffle submitted to rock avalanches based on discrete element method. Environ Earth Sci 80:600. https://doi.org/10.1007/s12665-021-09864-4

Xu Q, Shang Y, van Asch T et al (2012) Observations from the large, rapid Yigong rock slide – debris avalanche, southeast Tibet. Can Geotech J 49:589–606. https://doi.org/10.1139/t2012-021

Zhang B, Huang Y (2022) Effect of unsteady flow dynamics on the impact of monodisperse and bidisperse granular flow. Bull Eng Geol Environ 81:77. https://doi.org/10.1007/s10064-022-02573-7

Zhang B, Huang Y, Lu P, Li C (2020) Numerical investigation of multiple-impact behavior of granular flow on a rigid barrier. Water 12:3228. https://doi.org/10.3390/w12113228

Zhang B, Huang Y, Liu J (2021) Micro-mechanism and efficiency of baffle structure in deceleration of granular flows. Acta Geotech 16:3667–3688. https://doi.org/10.1007/s11440-021-01290-x

Zhang S, Yin Y, Li H et al (2022) Transport process and mechanism of the Hongshiyan rock avalanche triggered by the 2014 Ludian earthquake, China. Landslides 19:1987–2004. https://doi.org/10.1007/s10346-022-01878-8